PAPER

High performance tunnel field effect transistors based on in-plane transition metal dichalcogenide heterojunctions

IOP Publishing Nanotechnology
Nanotechnology 30 (2019) 025201 (11pp) https://doi.org/10.1088/1361-6528/aae7df

High performance tunnel field effect transistors based on in-plane transition metal dichalcogenide heterojunctions

Jean Choukroun[1], Marco Pala[1], Shiang Fang[2], Efthimios Kaxiras[2,3] and Philippe Dollfus[1]

[1] Centre for Nanoscience and Nanotechnology, CNRS, Univ. Paris Sud, Université Paris Saclay, Orsay, France
[2] Department of Physics, Harvard University, Cambridge, MA 02138, United States of America
[3] John A. Paulson School of Engineering and Applied Sciences, Harvard University, Cambridge, MA 02138, United States of America

E-mail: jean.choukroun@c2n.upsaclay.fr

Received 4 July 2018, revised 2 October 2018
Accepted for publication 12 October 2018
Published 1 November 2018

Abstract

In-plane heterojunction tunnel field effect transistors based on monolayer transition metal dichalcogenides are studied by means of self-consistent non-equilibrium Green's functions simulations and an atomistic tight-binding Hamiltonian. We start by comparing several heterojunctions before focusing on the most promising ones, i.e. WTe_2-MoS_2 and $MoTe_2$-MoS_2. The scalability of those devices as a function of channel length is studied, and the influence of backgate voltages on device performance is analyzed. Our results indicate that, by fine-tuning the design parameters, those devices can yield extremely low subthreshold swings (<5 mV/decade) and I_{ON}/I_{OFF} ratios higher than 10^8 at a supply voltage of 0.3 V, making them ideal for ultra-low power consumption.

Keywords: TFET, transition metal dichalcogenides, steep-slope, NEGF, tight-binding, quantum simulation, MoS_2

(Some figures may appear in colour only in the online journal)

1. Introduction

Power consumption is one the main limiting factors of progress in computing technologies, and the scaling of the power supply is the most effective approach to improve energy efficiency, as a tenfold reduction in V_{DD} results in a hundredfold save in dynamic power [1]. However, maintaining a high ON/OFF current (I_{ON}/I_{OFF}) with a lower power supply requires an extremely steep transition between the OFF and ON state of the device, which standard MOSFETs simply cannot provide due to their working mechanism.

Thanks to their ability to yield subthreshold swings (SS) below the thermionic limit of 60 mV/dec at room temperature that constrains MOSFETs [1, 2], Tunnel Field Effect Transistors (TFETs) are recognized to be one of the most promising avenues for the aforementioned scaling of the power supply (V_{DD}). However, since TFETs rely on a band-to-band tunneling (BTBT) mechanism, the current they provide in the ON-state is often several orders of magnitude lower than that of MOSFETs—depending on the length of the depletion region to be tunneled—which severely constrains the possible applications [3].

As will be detailed in section 3, thanks to the band-structure properties of the heterostructures investigated, the TFETs presented in this study do not suffer from this drawback and the I_{ON}/I_{OFF} ratios they present are actually higher than that of most MOSFETs. Encouraging experimental results have been reported in the case of Si and III–V semiconductor based TFETs [4–7], but the use of these materials entails a high concentration of traps and a high roughness at the interface, as well as dangling bonds, which all contribute and therefore decreasing the device performance [8–10]. The

use of TMD in TFETs is expected to be particularly beneficial in reducing the density of the interface traps, which are responsible for significant SS degradations and often prevent the experimental achievement of sub-thermionic swings. Moreover, in bulk materials, the quantum confinement arising from the nanoscale of the device widens the band gaps and prevents the formation of a truly broken band-gap heterostructure [11]. It is not the case for heterojunctions of 2D materials where, as described later, strain effects can actually induce a broken gap, which is most convenient for TFET performance, in particular in terms of I_{ON}.

Monolayer-based TFETs can be split into two categories: van der Waals TFETs, in which the monolayers are stacked vertically [12, 13], and conventional 'lateral' TFETs [14, 15], in which the monolayers occupy the same plane. Several in-plane 2D heterostructures have already been experimentally realized: from graphene-hBN [16–19] to graphene-monolayer transition metal dichalcogenide (TMD) [17, 20], to TMD–TMD [17, 21, 22], and the growth and deposition techniques related to 2D materials are rapidly expanding and becoming more versatile. Because of the aforementioned inherent advantages they hold when compared to bulk materials and of the recent advances in the techniques related to their experimental deposition, we elected to use in-plane 2D material heterostructures in the TFETs investigated. The materials used are monolayer TMDs: semi-conductors with band gaps ranging from ∼1 to 2 eV. Those materials as well as their reaction to strain were modeled via the tight-binding (TB) model detailed in section 2. In this article, we present atomistic quantum simulations of electronic transport in in-plane heterojunction TFETs based on TMDs as well as a pure WTe_2 TFET to be used as reference. Their transport characteristics (SS, I_{ON}/I_{OFF}) are then compared in order to select the most promising heterojunctions, which will be studied further. Namely, the influence of design parameters (backgate voltages, channel length) on their performance will be evaluated.

The paper is organized as follows: in section 2, the TB model and materials used are introduced, and the device structure and simulation methodology are described; in section 3, the simulation results for the pure WTe_2 TFET and all heterojunction TFETs are compared, while the most promising of these devices is studied further in section 4. Finally, conclusions and future works are addressed in section 4.

2. Device description and simulation methodology

2.1. Device description

All of the modeled TFETs share the same structure, which is shown in figure 1 (WTe_2-MoS_2 heterojunction in this case).

It features a monolayer TMD source, channel and drain, a 3.35 nm thick SiO_2 buried oxide and a high-ðœ top-gate oxide of equivalent oxide thickness $t_{oxe} = 0.44$ mm. In the case of the heterostructures, a first TMD acts as the source, while a second, different TMD is used in the channel and drain regions; the interface therefore lies between the source and the channel. Thanks to the 2D nature of the device, we can use backgates instead of chemical doping in order to control charge densities in the contacts, which allows for much more precise control over the behavior of the device and, contrary to chemical doping, does not introduce impurities in the material. Current flow through the device is controlled via a top-gate of length equal to the channel region.

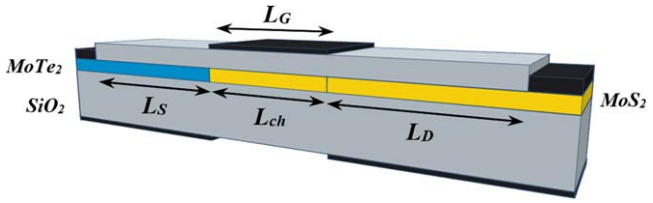

Figure 1. 3D sketch describing the structure of the studied TFETs (the $MoTe_2$-MoS_2 heterojunction is shown in this case). L_G, L_S, L_{ch}, and L_D are the gate, source, channel and drain lengths, respectively.

2.2. Material modeling methodology

While DFT studies of TMD-based devices have been recently reported [23, 24], in this work we adopted the empirical TB formalism in order to reduce the numerical burden of self-consistent quantum simulations. We consider five monolayer TMDs: MoS_2, $MoSe_2$, WSe_2, $MoTe_2$ and WTe_2, modeled using an 11-band TB model presented in [25], in which the effect of strain on the electronic properties is taken into account. It is worth noting that while WTe_2 and $MoTe_2$ were not included in those studies, the same work has since been done with those materials in order to obtain the necessary TB parameters. In this TB model, all the relevant orbitals near the Fermi level—i.e. the *p* orbitals for the chalcogen atoms and the *d* orbitals for metal atoms—are taken into account. The resulting TMDs are semi-conductors with direct band gaps ranging from 1.2 to 1.95 eV (see figure 2) located at the K-point of the Brillouin zone. Some relevant information regarding the pristine form of those materials can be found in table 1 (the reported lattice parameters were taken from [26, 27]).

Most *ab initio* studies [26–28] report lower band gaps for those materials because DFT notoriously underestimates band gaps [29]; as mentioned in the original article presenting the model, Green–Wannier calculations were performed to increase its accuracy, which explains the higher than average band gaps. In the case of heterojunction TFETs, some strain has to be applied to the materials in order to obtain lattice matching at the interface. Our TB model takes strain into account (see appendix for details), and therefore allows us to apply the necessary stress to the considered material and compute the resulting electronic properties.

In the case of $MoSe_2$-MoS_2 and WSe_2-MoS_2 TFETs, a 4.26% tensile strain has to be applied to MoS_2 in order to reach a lattice parameter of 3.32 Å (the same as the source material); in the case of the WTe_2-MoS_2 and $MoTe_2$-MoS_2 TFETs, a 5% tensile strain was applied onto MoS_2, while a 5% compressive strain was applied to the source material, in order to reach a lattice parameter of 3.35 Å along the whole device. In similar systems (like WSe_2-MoS_2), it has been

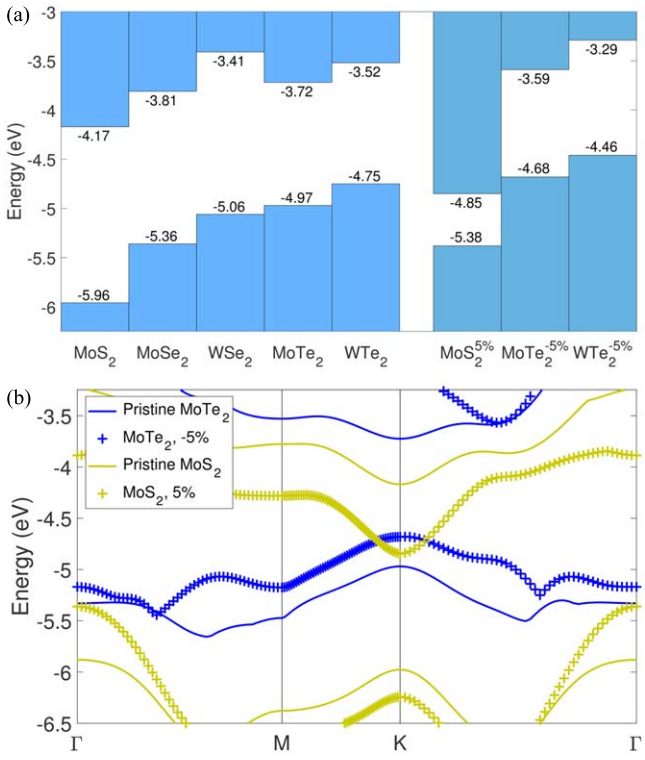

Figure 2. (a) Band alignment of the five considered TMDs, both in their pristine form (left) and when the strain needed in the heterostructures is applied (right). The vacuum level is set to 0 eV. It is worth noting that under these stresses, the band gaps become indirect in the considered materials. (b) Highest VB and lowest CB in pristine form (line) and under strain (crosses) for $MoTe_2$ (blue) and MoS_2 (gold). When the strains are applied, the top of the $MoTe_2$ VB is higher than the bottom of the MoS_2 CB, which is ideal for TFET operation.

Table 1. Physical parameters of considered TMDs in their pristine form. The band gaps are calculated from the TB Hamiltonian, and the lattice parameters are taken from [24, 25].

MX_2	MoS_2	WS_2	$MoSe_2$	WSe_2	$MoTe_2$	WTe_2
a (Å)	3.18	3.18	3.32	3.32	3.55	3.55
E_{gap} (eV)	1.79	1.95	1.55	1.65	1.25	1.23

shown that the strain at the interface is relaxed over several tens of nanometers [30]. The lead-to-lead distance in the devices investigated being shorter than the relaxation length, we have assumed that the relaxation can be neglected, which makes the atomistic simulation of the full device computationally tractable.

The effect of strain on the electronic properties of the considered TMDs (namely bad gap and alignment) is shown in figure 2(a), and more specifically on the band structure in the case of MoS_2 and $MoTe_2$ in figure 2(b). We can see that, in the case of the WTe_2-MoS_2 and $MoTe_2$-MoS_2 devices, the top of the source valence band (VB) is actually located at a higher energy than the bottom of the channel conduction band (CB) when we apply the necessary stress to reach lattice matching.

Because TFETs rely on BTBT, the alignment of the valence and CBs between the source and the channel region is paramount: it dictates the length of the depletion region the carriers will have to tunnel through to reach the channel, and therefore severely impacts the performance of the device (both SS and ON current). By lowering its CB by approximately 70 meV, applying the aforementioned 5% tensile strain on MoS_2 is highly beneficial to the devices investigated.

What is more, the 5% compressive strain on WTe_2 and $MoTe_2$ raises their VB by approximately 30 meV, so much so that they actually stand higher than the bottom of the MoS_2 CB; this configuration is known as a 'broken gap'. As will be shown in section 3, this is hugely beneficial to the device performance and is ideal for TFET operation, making the depletion region almost non-existent. It is worth noting that spin–orbit coupling is not included in this work, but is expected to raise the XTe_2 VB [31], increasing the overlap between the source VB and channel CB, and therefore benefiting the performance of the device.

2.3. Hamiltonian creation

As mentioned before, the TB model considers the p_x, p_y and p_z orbitals of the chalcogen atoms, and the d_{xy}, d_{xz}, d_{yz}, $d_{z^2-r^2}$ and $d_{x^2-y^2}$ of the metal atoms. As the unit cell (MX_2, represented in yellow in figure 3) is composed of one metal atom and two chalcogen atoms, the initial basis is an 11×11 matrix ($5d$ orbitals $+ 2 \times 3p$ orbitals). In order to use the non-equilibrium Green's function (NEGF) method, we need to describe the device as 'layers', repeating along the transport direction, which forces us to use a bigger unit cell than the one used in the original TB model. This new unit cell is represented in red in figure 3. It contains two metal atoms and four chalcogen atoms, and therefore leads to a 22×22 basis. Because of this change of unit cell, and of the way the model was introduced in the original article [25, 31], some adaptation work was required to create matrices describing the coupling between different orbitals based solely on the positions of the atoms they are associated with. From those matrices, 22×22 matrices describing the Hamiltonian of a single unit cell ($H_{n,m}$ in figure 3) and the coupling between this unit cell and an adjacent cell ($T_{i,j}$ in figure 3) are deduced. We only represent the coupling for half of the adjacent cells in order to preserve readability, but the coupling are symmetrical with respect to the original (n, m) unit cell, so that $T_{n-1,m-1} = T_{n+1,m+1}{}^{\dagger}$ for instance. The matrices describing the orbital couplings and the creation of the 22×22 Hamiltonians are given in appendix. At a given [k_x, k_y] wave vector, the 'layer' Hamiltonians can be calculated as shown in equations (1)–(3).

$$H_n(k_y) = H_{n,m} + T_{n,m+1}.e^{i.k_y.a_y} + T_{n,m-1}.e^{-i.k_y.a_y} \quad (1)$$

$$T_{n+1}(k_y) = T_{n+1,m} + T_{n+1,m-1}.e^{-i.k_y.a_y} + T_{n+1,m+1}.e^{i.k_y.a_y} \quad (2)$$

$$T_{n-1}(k_y) = T_{n+1}{}^{\dagger}(k_y) \quad (3)$$

From those Hamiltonians, the total Hamiltonian of the device is calculated as

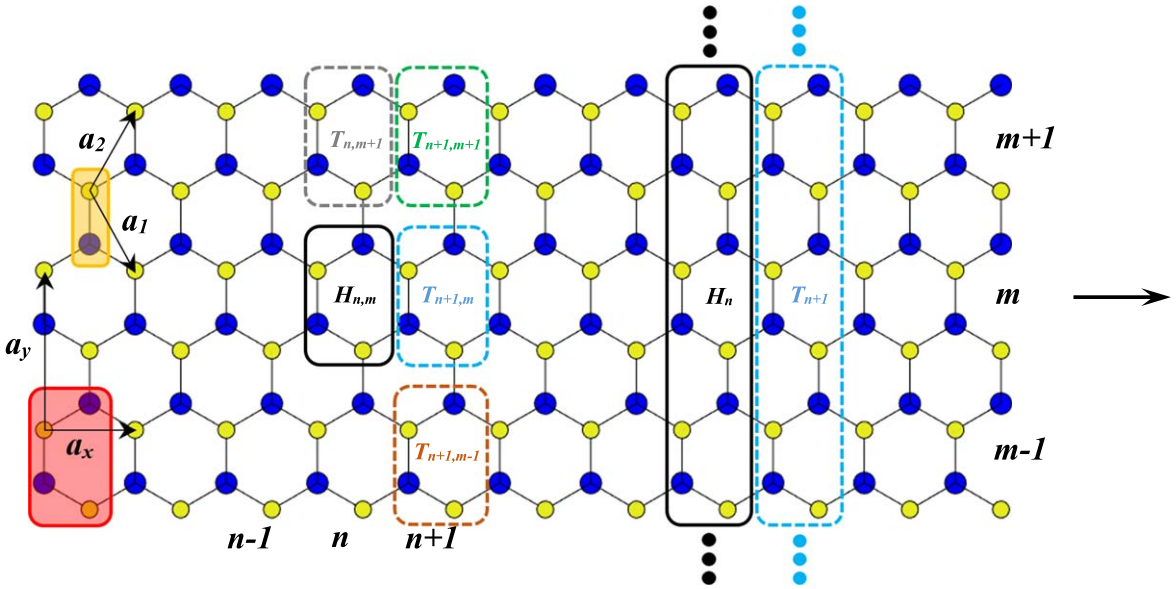

Figure 3. Atomic arrangement of TMDs. The yellow area represents the unit cell considered by the original TB model, and the red area represents the unit cell considered in our work. $H_{n,m}$ and H_n are the hamiltonians for a unit cell and single 'layer' of the material, respectively. Finally, $T_{i,j}$ and T_i represent the coupling of the (i), (j) cell with the (n), (m) cell, and of the (i) layer with the (n) layer, respectively. Transport direction is indicated by the arrow.

$$H_{tot}(k_x, k_y) = H_n(k_y) + T_{n+1}(k_y) \cdot e^{i.k_x.a_x} + T_{n-1}(k_y) \cdot e^{-i.k_x.a_x}. \quad (4)$$

This total Hamiltonian describes the 2D infinite TMD layer at a given wave vector. In the case of an in-plane heterojunction, the appropriate orbital couplings are used in each material, and the coupling at the interface is calculated as the average of the coupling parameters of the materials on either side of the interface. As an example, the ($n + 1$, m) coupling at the interface is calculated as ${T_{n+1,m}}^{A/B} = ({T_{n+1,m}}^{A} + {T_{n+1,m}}^{B})/2$ where $A(B)$ is the TMD on the left (right) of the interface.

2.4. Quantum simulation method

In this work, we use the NEGF [30, 31] method self-consistently coupled with 3D Poisson equation to compute ballistic electronic transport through the simulated devices. Once the aforementioned TB Hamiltonians have been generated, they can be used to calculate the device's Green function, from which we can calculate physical quantities such as current, charge, local density of states (LDOS)….

However, we use the Sancho–Rubio method [32] to calculate only the main diagonal and first sub-diagonal elements of the Green's function matrix, which are the only ones needed to obtain the physical quantities. This technique allows for an important reduction of the computational cost of those calculations, and is routinely used to simulate TFETs [33, 34].

As mentioned before, this NEGF method is self-consistently coupled with the solving of the 3D Poisson equation: an initial guess of the potential profile is used to calculate the device Hamiltonian, from which we can obtain the device's Green function. From this matrix, we can calculate the charge densities in the device, from which is then deduced an updated potential profile to be used as input for the calculation of the updated device's Green function. This loop is repeated until coherence is reached. Mean-free paths around 20 nm have been reported for MoS_2 [35], so, in the case of short devices, the ballistic approximation used here is expected to yield results comparable to those that would be obtained by including phonon scattering. Although the deformation potentials reported for TMDs are relatively small [36–38], phonon scattering will undoubtedly slightly impact performance in the case of devices of length exceeding 20 nm, by increasing SS—due to a widening of the density of states—, and decreasing ON current. Similarly, the impact of the crystallinity on the performance of such devices is expected to be negligible, because typical domain size in TMD materials is larger than the devices considered in this work [39, 40].

3. Results and discussion

In the following discussion of the results we will often refer to a specific metric to describe the performance of the investigated TFETs: their SS. This metric is expressed in mV/dec, and describes the increase in gate voltage needed to increase the current tenfold, which is why the lower the SS, the steeper the slope. The SS of a logic device therefore relates to the steepness of the slope of the I_{DS}–V_G characteristic at low V_G. Due to their working mechanism and the Fermi–Dirac distribution they are bound to, MOSFETs physically cannot provide SS below 60 mV/dec. Because TFETs rely on BTBT, they have no theoretical limit for SS and can approach the behavior of an ideal switch: to be in a fully OFF state at a given V_G, and in a fully ON state at an infinitesimally higher $V_G + \delta V_G$. This would allow for extremely fast and easy switching, requiring a minimal amount of energy. In this

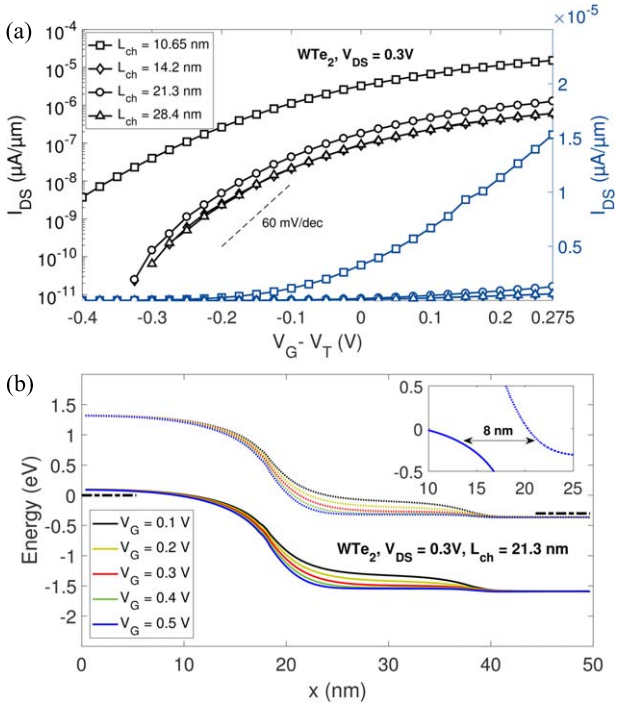

Figure 4. (a) I_{DS}–V_G characteristics of the pure WTe_2 device. (b) Highest CB and lowest VB for V_G ranging from 0.1 to 0.5 V; inset: zoom on the interface for $V_G = 0.5$ V. Both figures were obtained at $V_{DS} = 0.3$ V, $V_{BG-S} = -1.35$ V, and $V_{BG-D} = -0.75$ V.

work, SS is calculated as the average swing between $I_{DS} = 10^{-5}$ and $10^{-2}\,\mu\text{A}\,\mu\text{m}^{-1}$. The ON current, I_{ON}, is defined as the current at a gate voltage $V_{ON} = V_{OFF} + V_{DS}$, where V_{OFF} is the gate voltage at which the value for the selected OFF current (in our case $10^{-5}\,\mu\text{A}\,\mu\text{m}^{-1}$) is reached, and V_{DS} is the drain bias applied to the device. The goal of the studied TFETs is therefore to provide the lowest SS and highest I_{ON}/I_{OFF} ratio possible.

3.1. Pure WTe_2 TFET

Before studying in-plane TMD heterojunctions, we simulated a pure WTe_2 TFET so that it can be used as a point of reference and as comparison for the heterojunction based devices. We elected to use WTe_2 because it has the lowest band gap out of the five considered TMDs (1.23 eV in the TB model used), and should therefore have the shortest depletion region in the ON state and, subsequently, should present the highest performances.

The WTe_2 TFET was studied at backgate voltages of $V_{BG-S} = -1.25$ V, $V_{BG-D} = -0.75$ V, at a supply voltage of $V_{DS} = 0.3$ V, and has a 17.75 nm long source, a 10.65 nm long drain, and a channel length ranging from 10 to 29 nm. The corresponding I_{DS}–V_G characteristics are shown in figure 4(a), in which the threshold voltage (V_T) was obtained via the linear approximation of the ON state current. These characteristics highlight the poor performance of this pure WTe_2 device: the SS is higher than 60 mV/dec for all channel lengths considered, and low ON currents reaching only $10^{-5}\,\mu\text{A}\,\mu\text{m}^{-1}$ for the 10 nm channel, and $10^{-7}\,\mu\text{A}\,\mu\text{m}^{-1}$ for the longer ones. Figure 4(b), which shows the highest VB and lowest CB in this device for several gate voltages at $L_{ch} = 21.3$ nm, highlights the origin of these poor performances. Even at a high gate voltage of $V_G = 0.5$ V, the depletion region the carriers have to tunnel through is approximately 8 nm long, which is too high for any significant current to take place. While it is the lowest band gap out of the five TMDs, the 1.23 eV gap of WTe_2 is too high and severely hampers the prospects of a pure WTe_2 device.

It is worth noting that several other works on similar devices have reported better performances [15, 41, 42], which can be attributed to the fact that, as mentioned in the presentation of the TB model, the 1.23 eV band gap calculated in this work is higher than routinely obtained DFT values, which usually underestimate the actual band gap [29].

3.2. Comparison of all heterojunction TFETs

The in-plane heterojunctions investigated are $MoSe_2$-MoS_2, WSe_2-MoS_2, $MoTe_2$-MoS_2 and WTe_2-MoS_2. As a reminder, MoS_2 is under a 4.2% tensile strain in the XSe_2-MoS_2 devices to reach $a_{Se} = 3.32$ Å; in the XTe_2-MoS_2 devices, MoS_2 is under a 5.3% tensile strain, while WTe_2 and $MoTe_2$ are under a 5.6% compressive stress, in order to reach a common lattice parameter of $a_{Te} = 3.35$ Å.

For the sake of clarity, the lengths mentioned in this part are rounded off, so that they apply to all devices. Figure 5(a) shows the LDOS, as well as the highest VB and lowest CB for all devices in the ON state, at a gate voltage of $V_G = 0.4$ V, a supply voltage of $V_{DS} = 0.3$ V, and lengths of $L_S = L_D = 17$ nm and $L_{ch} = 27$ nm. These LDOS figures give a clear picture of the depletion region the carriers have to tunnel through in the ON state, and highlights the benefits of the 'broken gap' configuration found in the $MoTe_2$-MoS_2 and the WTe_2-MoS_2 devices: the depletion region is almost non-existent in those devices, which explains their outstanding performance, shown in figure 5(b). This figure represents the I_{Ds}–V_G characteristics of the pure WTe_2 and all heterojunction devices: the direct correlation between the length of the depletion region and the performance of the device is obvious; the XSe_2-MoS_2 devices show very low ON current and very high SS, due to their approximately 5 nm long depletion region.

Out of those two, WSe_2-MoS_2 has the best performance, with a steeper slope in the OFF regime, and an ON current roughly 100 times higher than that of $MoSe_2$-MoS_2 TFET; with that said, its I_{ON}/I_{OFF} ratio (2×10^4) is too low to realistically envision logic applications.

On the other hand, it is obvious from those characteristics that the XTe_2-MoS_2 devices are far more promising. They showcase an extremely steep slope in the OFF regime which leads to a <5 mV/dec SS in both devices, and very high ON currents of roughly $10^3\,\mu\text{A}\,\mu\text{m}^{-1}$ in the case of $MoTe_2$-MoS_2, and $2 \times 10^3\,\mu\text{A}\,\mu\text{m}^{-1}$ in the case of WTe_2-MoS_2. The band offsets, depletion region lengths, I_{ON}/I_{OFF} ratios and SS for all four heterojunction devices are summarized in table 2.

Due to their show extremely promising performance (very low SS and high I_{ON}/I_{OFF} ratio), the $MoTe_2$-MoS_2 and WTe_2-MoS_2 devices need to be studied more fully. For the $MoTe_2$-MoS_2 system especially, we will investigate the

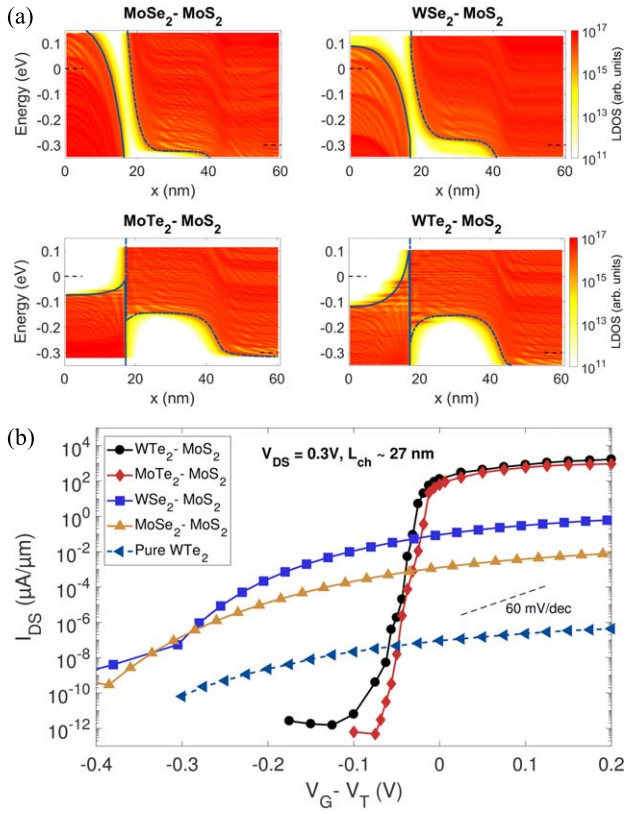

Figure 5. (a) LDOS at $V_G = 0.4$ V for all four heterojunction devices. (b) I_{DS}–V_G characteristics for the pure WTe_2 TFET and all four heterojunction TFETs at $V_{DS} = 0.3$ V, $L_S = L_D = 17$ nm and $L_{ch} = 27$ nm.

Table 2. Band offsets (channel CB minimum—source VB maximum) and transport properties of the TFETs, at $V_{DS} = 0.3$ V. $L_{depletion}$ was calculated at $V_G = 0.4$ V.

Source MX_2	$MoSe_2$	WSe_2	$MoTe_2$	WTe_2
Band offset (eV)	0.65	0.35	−0.17	−0.39
$L_{depletion}$ (nm)	5.3	4.6	∼0	∼0
I_{ON}/I_{OFF}	9×10^2	2×10^4	10^8	2×10^8
SS (mV/dec)	150	50	<5	<5

influence of design parameters such as channel length and backgate voltages on the device performance. The study of the WTe_2-MoS_2 device leading to very similar results, it is mentioned but not fully detailed here.

3.3. Study of the $MoTe_2$-MoS_2 heterojunction TFET

We start by studying the scaling of this device with respect to channel length, and its influence on transport properties. I_{DS}–V_G characteristics for channel lengths ranging from 10 to 27 nm are shown in figure 6(a), while figure 6(b) highlights the impact of channel length on SS and ON current in this device. The current characteristics show the high impact of channel length on the steepness of the slope in the OFF regime: due to increased electrostatic integrity in longer channels, SS decreases from 60 mV/dec in the case of a short 7.4 nm channel to approximately 3 mV/dec when channel length exceeds 20 nm.

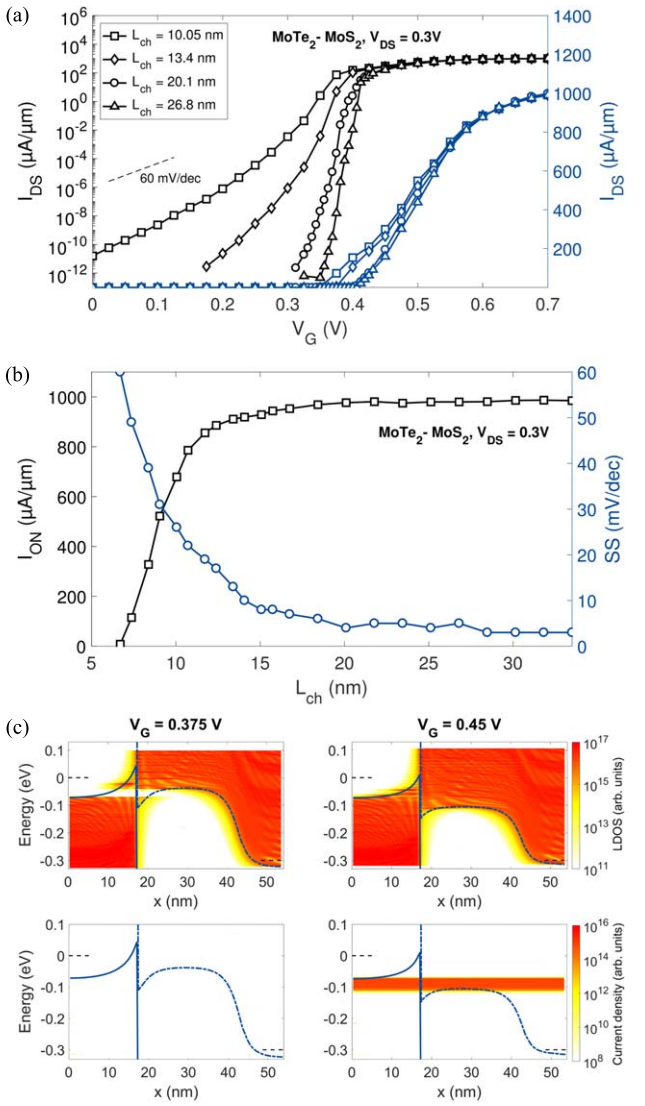

Figure 6. (a) I_{DS}–V_G characteristics for the $MoTe_2$-MoS_2 TFET for several channel lengths. (b) Influence of channel length on SS and ON current in this TFET. (c) LDOS and current density in the OFF (left) and ON (right) state for the TFET at $L_{ch} = 20.1$ nm; the highest VB (full lines) and lowest CB (dashed lines) along the device are also shown. In all figures, $V_{DS} = 0.3$ V, $V_{BG-S} = 0.58$ V and $V_{BG-D} = 0.8$ V.

The current behaves similarly at high gate voltages no matter the channel length, contrary to V_{OFF}—the gate voltage at which $I_D = I_{OFF} = 10^{-5}\,\mu A\,\mu m^{-1}$—, which is highly impacted. Therefore the ON current, calculated at $V_{ON} = V_{OFF} + V_{DS}$, increases with channel length until reaching a plateau around $10^3\,\mu A\,\mu m^{-1}$ for channel lengths exceeding 17 nm. LDOS and current densities for the 20.1 nm channel device are shown in figure 6(c), and highlight the extremely low SS of this device. At $V_G = 0.375$ V, the device is in a fully OFF state, as evidenced by the LDOS 'gap' at the interface between −0.04 and −0.06 eV, and by a current density 8 orders of magnitude lower than in the ON state.

At $V_G = 0.45$ V however, the device is in a fully ON state and current flows freely from the source to the drain, as represented in the current density figure. As mentioned when

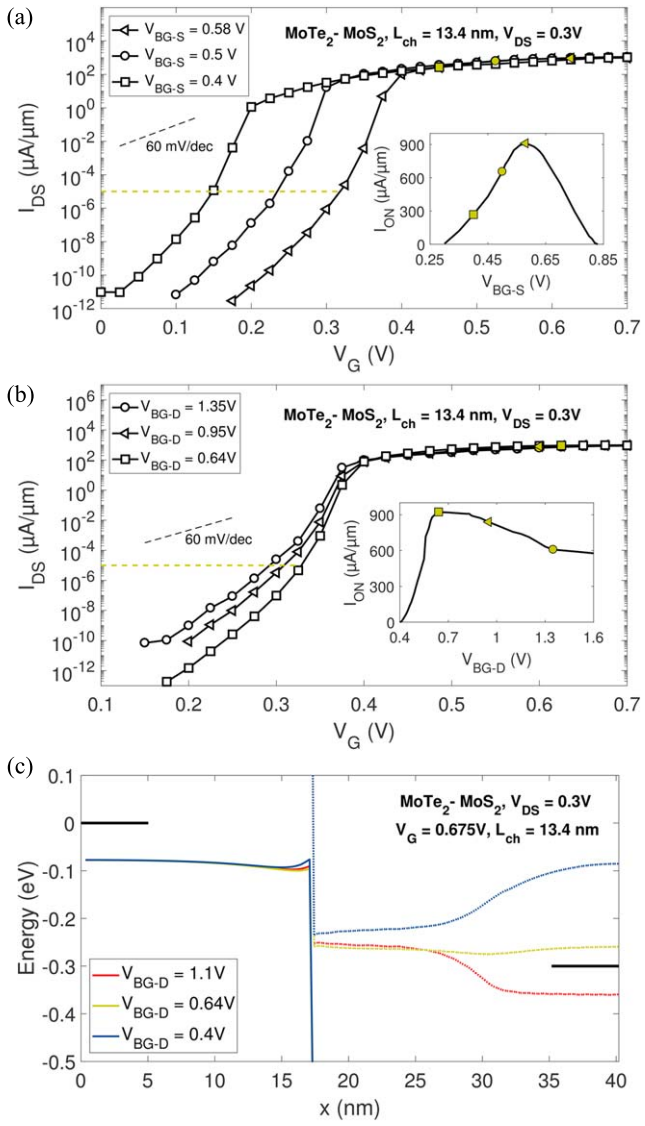

Figure 7. (a) I_{DS}–V_G characteristics for the $MoTe_2$-MoS_2 TFET for several source backgate voltages at $V_{BG-D} = 0.8$ V. Inset: influence of source backgate voltage on I_{ON}. (b) I_{DS}–V_G characteristics for the $MoTe_2$-MoS_2 TFET for several drain backgate voltages at $V_{BG-S} = 0.58$ V. Inset: influence of drain backgate voltage on I_{ON}. In both (a) and (b) figures, the yellow dashed line indicates $I_{OFF} = 10^{-5}\ \mu A\ \mu m^{-1}$, and the yellow markers indicate the ON current calculated at $V_{ON} = V_{OFF} + V_{DS}$. (c) Highest VB (full lines) and lowest CB (dashed lines) for the device shown in (b), at several V_{BG-D}, and $V_G = 0.675$ V.

we described the structure of the device investigated, we elected to use backgates to electrostatically control charge densities in the contacts instead of chemical doping. Those backgates therefore directly control the energy states in the contacts, and are expected to be an important tuning parameter in this device.

We will now study the influence of the source and drain backgate voltages on the performance of the $MoTe_2$-MoS_2 device with $L_{ch} = 13.4$ nm and $V_{DS} = 0.3$ V. Figure 7(a) shows the current characteristics for this device at $V_{BG-D} = 0.8$ V and several source backgate voltages ranging from 0.4 to 0.58 V, and the inset highlights the influence of V_{BG-S} on the device's ON current. As we can see from the main figure, while V_{BG-S} has no impact on SS, it highly controls the threshold voltage and therefore V_{ON}. The inset clearly shows a somewhat parabolic influence of source backgate voltage on ON current, with an optimal voltage range from approximately 0.55 to 0.6 V.

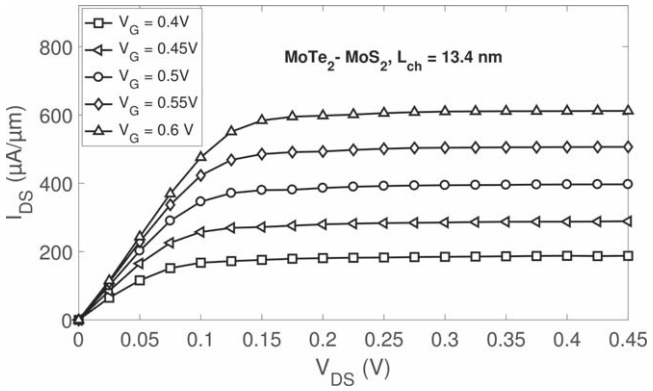

Figure 8. I_{DS}–V_{DS} characteristics for the $MoTe_2$-MoS_2 TFET at several gate voltages ranging from $V_G = 0.35$ V to $V_G = 0.6$ V, at $V_{BG-S} = 0.4$ V and $V_{BG-D} = 2.85$ V.

A similar study about the influence of drain backgate voltage was performed on the same device at a fixed $V_{BG-S} = 0.58$ V. As is shown in figure 7(b), V_{BG-D} also has a strong impact on the current characteristics of this device: SS decreases as we lower the drain backgate voltage, while the ON current increases to reach a maximum of approximately $9 \times 10^2\ \mu A\ \mu m^{-1}$ around $V_{BG-D} = 0.65$ V. However, by decreasing the drain backgate voltage further, the CB in the drain is pulled towards higher energies, reducing the width of the tunneling window and therefore the ON current. As is shown in figure 7(c), the drain CB actually rests higher than the source VB at $V_{BG-D} = 0.4$ V, which explains the absence of current. The optimal drain backgate voltage therefore depends on the applied source backgate voltage. We can conclude from this study that the optimal voltages to apply to the backgates to operate this in-plane $MoTe_2$-MoS_2 TFET at $V_{DS} = 0.3$ V are $V_{BG-S} = 0.58$ V and $V_{BG-D} = 0.64$ V.

Figure 8 shows the I_{DS}–V_{DS} characteristics of the 13.4 nm channel device at several gate voltages ranging from $V_G = 0.35$ V to $V_G = 0.6$ V. The current increases linearly with the applied gate voltage, and current saturation is reached around $V_{DS} = 0.2$ V; this indicates that the device can operate at its full capacity even at low drain biases, which makes its use for ultra-low power operation even greater.

As presented, we were able to determine the optimal design parameters for this TFET in order to maximize its performance. By using a channel length of at least 20 nm and the aforementioned optimal backgate voltages, this device can yield a SS below 5 mV/dec and an I_{ON}/I_{OFF} ratio of 10^8. Those performances are far greater than those reported in other 2D material heterojunction based TFETs [4, 11, 15, 41].

Although the results are not shown here, the same study was performed on the WTe_2-MoS_2 TFET and similar results were obtained: the influence of channel length on SS and ON

current is the same, and the optimal backgate voltages at $V_{DS} = 0.3$ V for this device are found to be $V_{BG-S} = 0.85$ V and $V_{BG-D} = 0.65$ V. Under those conditions the WTe_2-MoS_2 TFET can yield SS below 5 mV/dec and ON currents beyond $2 \times 10^8\ \mu A\ \mu m^{-1}$.

4. Conclusion

By means of an atomistic TB approach and self-consistent quantum simulations, we investigated several types of in-plane 2D material heterojunction based TFETs. Band alignment was highlighted as one of the most important parameters for TFET operation, and the influence of several design parameters on device performance was studied. Through careful selection of the materials system, channel length and backgate voltages, SS below 5 mV/dec and high I_{ON}/I_{OFF} ratios ($>10^8$) were reported at a low drain bias of 0.3 V. Those in-plane heterojunction TFETs are therefore ideal candidates for ultra-low power operation.

Acknowledgments

SF and EK were supported by the STC Center for Integrated Quantum Materials, NSF Grant No. DMR-1231319 and by ARO MURI Award W911NF-14-0247.

Appendix

In this appendix, we describe the creation of the TB Hamiltonians referred to in the body of the article.

For more in-depth information about the creation of the TB model itself and the way strain is handled, we refer the reader to the original article describing the model [25].

The details provided in this appendix are to be used in conjunction with the original article due to recurring notations and notions, and callbacks to parameters and calculations found in the article describing the TB model.

The 11×11 basis used to describe a single MX_2 unit cell in this TB model is the following

$$|d_{xz}\rangle,\ |d_{yz}\rangle,\ |p_x\rangle,\ |p_y\rangle,\ |p_z\rangle,\ |d_{xy}\rangle,\ |d_{x^2-y^2}\rangle,$$
$$|d_{z^2}\rangle,\ |p_x\rangle,\ |p_y\rangle,\ |p_z\rangle.$$

It contains the five *d* orbitals of the metal atom as well as the three *p* orbitals of each chalcogen atom, and is arranged as such due to symmetry considerations with respect to a *xy* mirror plane.

The original article describes the calculation of the 11×11 coupling Hamiltonians depending on the strain applied, and of the final, total Hamiltonian. However, as mentioned in section 2, the use of a NEGF method requires a unit cell that can be reproduced along the transport direction, which is not the case of the basic MX_2 unit cell used in the TB model. We therefore use a unit cell that is twice the size of the original one, and will result in 22×22 Hamiltonians. In order to construct those Hamiltonians, we created matrices that describe the coupling between orbitals depending on the relative positions of the atoms they are associated with. There are nine 'position pairs' leading to a coupling between orbitals and therefore nine such matrices, referred to as δ_1–δ_9 and shown in figure A1.

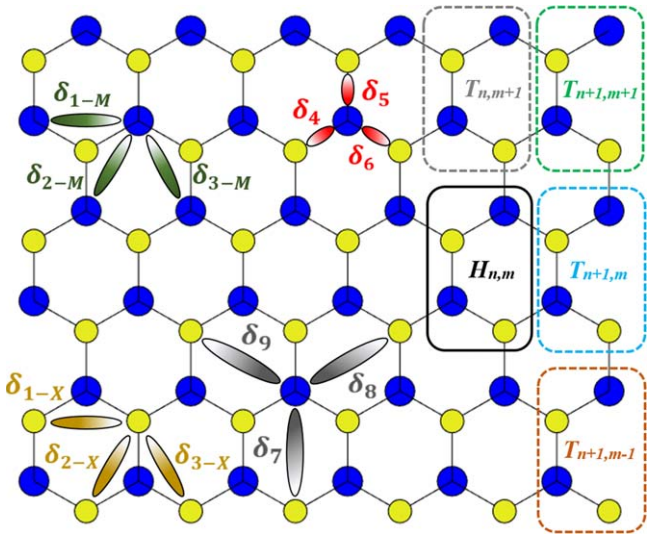

Figure A1. Lattice arrangement of a TMD. The highlighted δ_1 through δ_9 areas represent the coupling matrices between various orbitals on the considered atoms.

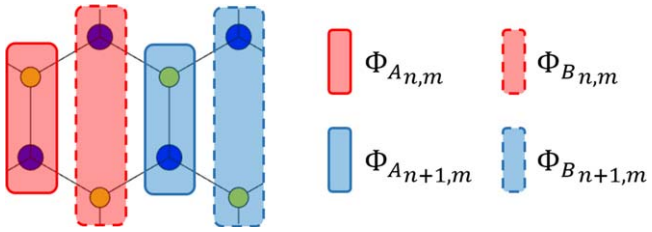

Figure A2. Visualization of the A and B sublattices in two adjacent unit cells. Dashed (full) lines represent the A (B) sublattice, and their color indicates the unit cell to which they belong (red for the (n, m) unit cell, blue for the $(n + 1, m)$ unit cell).

In this figure, the direction of the coupling follows the color gradient (for instance, δ_4–δ_9 represent the coupling from the X to the M atom).

The δ_i matrices are 11×11 matrices and are deduced from the Hamiltonians presented in the original article.

- δ_1, δ_2 and δ_3 represent the coupling between orbitals located on atoms of the same type: either M–M or X–X coupling; they are split into separate δ_{i-X} and δ_{i-M} matrices to simplify Hamiltonian construction later on.
- δ_4, δ_5 and δ_6 represent the first-neighbor coupling between orbitals located on atoms of a different type (X–M coupling).
- δ_7, δ_8 and δ_9 represent the third-neighbor coupling between orbitals located on atoms of a different type (X–M coupling).

The δ_{1-X}, δ_{1-M}, δ_5 and δ_7 matrices are calculated from the Hamiltonians given in the original article as follows, where $H^{(n)}_{XY\,ij}$ is the $(i,\ j)$ element of the $H^{(n)}_{XY}$ matrix.

$$\delta_{1-X} = \begin{bmatrix}
0&0&0&0&0&0&0&0&0&0&0\\
0&0&0&0&0&0&0&0&0&0&0\\
0&0&H^{(2)}_{BB\,11}&H^{(2)}_{BB\,21}&H^{(2)}_{BB\,31}&0&0&0&0&0&0\\
0&0&H^{(2)}_{BB\,12}&H^{(2)}_{BB\,22}&H^{(2)}_{BB\,32}&0&0&0&0&0&0\\
0&0&H^{(2)}_{BB\,13}&H^{(2)}_{BB\,23}&H^{(2)}_{BB\,33}&0&0&0&0&0&0\\
0&0&0&0&0&0&0&0&0&0&0\\
0&0&0&0&0&0&0&0&0&0&0\\
0&0&0&0&0&0&0&0&0&0&0\\
0&0&0&0&0&0&0&0&H^{(2)}_{DD\,11}&H^{(2)}_{DD\,21}&H^{(2)}_{DD\,31}\\
0&0&0&0&0&0&0&0&H^{(2)}_{DD\,12}&H^{(2)}_{DD\,22}&H^{(2)}_{DD\,32}\\
0&0&0&0&0&0&0&0&H^{(2)}_{DD\,13}&H^{(2)}_{DD\,23}&H^{(2)}_{DD\,33}
\end{bmatrix}$$

$$\delta_{1-M} = \begin{bmatrix}
H^{AA\,(2)}_{11}&H^{AA\,(2)}_{21}&0&0&0&0&0&0&0&0&0\\
H^{AA\,(2)}_{12}&H^{AA\,(2)}_{22}&0&0&0&0&0&0&0&0&0\\
0&0&0&0&0&0&0&0&0&0&0\\
0&0&0&0&0&0&0&0&0&0&0\\
0&0&0&0&0&0&0&0&0&0&0\\
0&0&0&0&0&H^{CC\,(2)}_{11}&H^{CC(2)}_{21}&H^{CC\,(2)}_{31}&0&0&0\\
0&0&0&0&0&H^{CC\,(2)}_{12}&H^{CC\,(2)}_{22}&H^{CC\,(2)}_{32}&0&0&0\\
0&0&0&0&0&H^{CC\,(2)}_{13}&H^{CC\,(2)}_{23}&H^{CC\,(2)}_{33}&0&0&0\\
0&0&0&0&0&0&0&0&0&0&0\\
0&0&0&0&0&0&0&0&0&0&0\\
0&0&0&0&0&0&0&0&0&0&0
\end{bmatrix}$$

$$\delta_5 = \begin{bmatrix}
0&0&0&0&0&0&0&0&0&0&0\\
0&0&0&0&0&0&0&0&0&0&0\\
H^{(1)}_{BA\,11}&0&0&0&0&0&0&0&0&0&0\\
0&H^{(1)}_{BA\,22}&0&0&0&0&0&0&0&0&0\\
0&H^{(1)}_{BA\,32}&0&0&0&0&0&0&0&0&0\\
0&0&0&0&0&0&0&0&0&0&0\\
0&0&0&0&0&0&0&0&0&0&0\\
0&0&0&0&0&0&0&0&0&0&0\\
0&0&0&0&0&H^{(1)}_{DC\,11}&0&0&0&0&0\\
0&0&0&0&0&0&H^{(1)}_{DC\,22}&H^{(1)}_{DC\,23}&0&0&0\\
0&0&0&0&0&0&H^{(1)}_{DC\,32}&H^{(1)}_{DC\,33}&0&0&0
\end{bmatrix}$$

$$\delta_7 = \begin{bmatrix}
0&0&0&0&0&0&0&0&0&0&0\\
0&0&0&0&0&0&0&0&0&0&0\\
0&0&0&0&0&0&0&0&0&0&0\\
0&0&0&0&0&0&0&0&0&0&0\\
0&0&0&0&0&0&0&0&0&0&0\\
0&0&0&0&0&0&0&0&0&0&0\\
0&0&0&0&0&0&0&0&0&0&0\\
0&0&0&0&0&0&0&0&0&0&0\\
0&0&0&0&0&H^{(3)}_{DC\,11}&0&0&0&0&0\\
0&0&0&0&0&0&H^{(3)}_{22}{}^{DC}&H^{(3)}_{23}{}^{DC}&0&0&0\\
0&0&0&0&0&0&H^{(3)}_{32}{}^{DC}&H^{(3)}_{33}{}^{DC}&0&0&0
\end{bmatrix}.$$

Due to the three-fold rotational symmetry of TMDs, all other δ_i matrices can be deduced from these four matrices via the transfer matrix ${A_R}^{3\times3}$, which describes a $\frac{2\pi}{3}$ counter-clockwise rotation.

$${A_R}^{3\times3} = \begin{bmatrix} -1/2 & \sqrt{3}/2 & 0 \\ -\sqrt{3}/2 & -1/2 & 0 \\ 0 & 0 & 1 \end{bmatrix}.$$

And can be transformed into a 11×11 matrix as such

$$U_R = \begin{bmatrix}
-1/2 & -\sqrt{3}/2 & 0 & 0 & 0\\
-\sqrt{3}/2 & -1/2 & 0 & 0 & 0\\
0 & 0 & {A_R}^{3\times3} & 0 & 0\\
0 & 0 & 0 & {A_R}^{3\times3} & 0\\
0 & 0 & 0 & 0 & {A_R}^{3\times3}
\end{bmatrix}.$$

Therefore, we can calculate some of the remaining δ_i matrices as follows

$$\delta_3 = \langle {U_R}^{\dagger}|\ \delta_1|U_R\rangle,\ \ \delta_4 = \langle {U_R}^{\dagger}|\ \delta_5|U_R\rangle,\ \delta_8 = \langle {U_R}^{\dagger}|\ \delta_7|U_R\rangle$$

and, by applying the same rotation operation, we can obtain all remaining δ_i matrices

$${\delta_2}^{\dagger} = \langle {U_R}^{\dagger}|\delta_3|U_R\rangle,\ \ \delta_6 = \langle {U_R}^{\dagger}|\delta_4|U_R\rangle,\ \delta_9 = \langle {U_R}^{\dagger}|\ \delta_8|U_R\rangle.$$

It is worth noting that by applying U_R on δ_3, we obtain ${\delta_2}^{\dagger}$ and not δ_2 because, due to the way the vectors were defined (see figure 8), $\overrightarrow{\delta_3}$ becomes $-\overrightarrow{\delta_2}$ via this $\frac{2\pi}{3}$ counter-clockwise rotation.

Now that all of the δ_i matrices have been calculated from parameters and Hamiltonians given in the original article, only the on-site energies remain to consider before we can construct the 22×22 Hamiltonians.

These on-site energies are the elements of the $H^{(0)}_{ii}$ matrices found in the original article, which we gather in a 11×11 diagonal matrix E_i, of which the diagonal element is

$$[H^{(0)}_{AA\,11}\ H^{(0)}_{AA\,22}\ H^{(0)}_{BB\,11}\ H^{(0)}_{BB\,22}\ H^{(0)}_{BB\,33}\ H^{(0)}_{CC\,11}\cdots$$
$$\cdots\ H^{(0)}_{CC\,22}\ H^{(0)}_{CC\,33}\ H^{(0)}_{DD\,11}\ H^{(0)}_{DD\,22}\ H^{(0)}_{DD\,33}].$$

With all δ_i matrices and the on-site energies E_i now calculated, the 22×22 Hamiltonians describing the $(MX_2)_2$ unit cell and its coupling with neighboring cells can be constructed.

Because the unit cell considered is twice the size of the original unit cell, two sublattices A and B (shown in figure A2) can be distinguished in each cell. Each of them is associated to an 11×11 basis

$$\Phi_A = |d_{xz}\rangle,\ |d_{yz}\rangle,\ |p_x\rangle,\ |p_y\rangle,\ |p_z\rangle,\ |d_{xy}\rangle,\ |d_{x^2-y^2}\rangle,$$
$$|d_{z^2}\rangle,\ |p_x\rangle,\ |p_y\rangle,\ |p_z\rangle$$
$$\Phi_B = |d_{xz}\rangle,\ |d_{yz}\rangle,\ |p_x\rangle,\ |p_y\rangle,\ |p_z\rangle,\ |d_{xy}\rangle,\ |d_{x^2-y^2}\rangle,$$
$$|d_{z^2}\rangle,\ |p_x\rangle,\ |p_y\rangle,\ |p_z\rangle.$$

Each 22 × 22 Hamiltonian is therefore composed of four 11 × 11 matrices $\Psi_{X_{i,j}.Y_{k,l}}$. Those matrices are linear combinations of the δ_i and E_i matrices, and describe the coupling between the X sublattice of the (i, j) unit cell and the Y sublattice of the (k, l) unit cell. They can be constructed by studying figure 8 and selecting the appropriate couplings based on the atomic positions considered.

$H_{n,m}$ (the Hamiltonian of the unit cell) and $T_{i,j}$ (the Hamiltonians describing the coupling between the unit cell and adjacent cells), can be constructed as

$$H_{n,m} = \begin{pmatrix} \Psi_{A_{n,m}.A_{n,m}} & \Psi_{B_{n,m}.A_{n,m}} \\ \Psi_{A_{n,m}.B_{n,m}} & \Psi_{B_{n,m}.B_{n,m}} \end{pmatrix}$$

$$T_{i,j} = \begin{pmatrix} \Psi_{A_{n,m}.A_{i,j}} & \Psi_{B_{n,m}.A_{i,j}} \\ \Psi_{A_{n,m}.B_{i,j}} & \Psi_{B_{n,m}.B_{i,j}} \end{pmatrix}$$

with $i = [n-1, n, n+1]$ and $j = [m-1, m, m+1]$.

Therefore, the final, 22 × 22 Hamiltonians describing each TMD are calculated as follows

$$H_{n,m} = \begin{pmatrix} E_i + \delta_5 + \delta_5{}^\dagger & \delta_6{}^\dagger + \delta_4 + \delta_{3-X} + \delta_{2-M}{}^\dagger \\ \delta_6 + \delta_4{}^\dagger + \delta_{3-X}{}^\dagger + \delta_{2-M} & E_i + \delta_7 + \delta_7{}^\dagger \end{pmatrix}$$

$$T_{n+1,\,m} = \begin{pmatrix} \delta_{1-X}{}^\dagger + \delta_{1-M}{}^\dagger + \delta_8{}^\dagger + \delta_9 & 0 \\ \delta_{3-M} + \delta_{2-X}{}^\dagger + \delta_6{}^\dagger + \delta_4 & \delta_{1-X}{}^\dagger + \delta_{1-M}{}^\dagger \end{pmatrix}$$

$$T_{n+1,\,m-1} = \begin{pmatrix} 0 & 0 \\ \delta_{3-X} & \delta_9 \end{pmatrix} \quad T_{n+1,m+1} = \begin{pmatrix} 0 & 0 \\ \delta_{2-M}{}^\dagger & \delta_8{}^\dagger \end{pmatrix}$$

$$T_{n,\,m+1} = \begin{pmatrix} \delta_7 & \delta_{2-X}{}^\dagger \\ \delta_{3-M}{}^\dagger & \delta_5{}^\dagger \end{pmatrix} \quad T_{n-k,m-l} = T_{n+k,m+l}{}^\dagger.$$

ORCID iDs

Jean Choukroun https://orcid.org/0000-0001-7647-4980

References

[1] Esseni D, Pala M, Palestri P, Alper C and Rollo T 2017 A review of selected topics in physics based modeling for tunnel field-effect transistors *Semicond. Sci. Technol.* **32** 083005

[2] Cheung K P 2010 On the 60 mV/dec @300 K Limit for MOSFET subthreshold swing *IEEE Explore Proc. of 2010 Int. Symp. on VLSI Technology, System and Application* 72–3

[3] Avci U E, Morris D H and Young I A 2015 Tunnel field-effect transistors: prospects and challenges *IEEE J. Electron Devices Soc.* **3** 88–95

[4] Dey A W *et al* 2013 High-current GaSb/InAs(Sb) nanowire tunnel field-effect transistors *IEEE Electron Device Lett.* **34** 211–3

[5] Mohata D *et al* 2012 Barrier-engineered arsenide–antimonide heterojunction tunnel FETs with enhanced drive current *IEEE Electron Device Lett.* **33** 1568–70

[6] Dewey G *et al* 2011 Fabrication, characterization, and physics of III–V heterojunction tunneling field effect transistors (H-TFET) for steep sub-threshold swing *IEEE Explore 2011 Int. Electron Devices Meeting* 1–33

[7] Carrillo-Nunez H, Luisier M and Schenk A 2015 Analysis of InAs-Si heterojunction nanowire tunnel FETs: extreme confinement versus bulk *Solid-State Electron.* **113** 61–7

[8] Pala M G and Esseni D 2013 Interface traps in InAs nanowire tunnel-FETs and MOSFETs: I. Model description and single trap analysis in tunnel-FETs *IEEE Trans. Electron Devices* **60** 2795–801

[9] Esseni D and Pala M G 2013 Interface traps in InAs nanowire tunnel FETs and MOSFETs: II. Comparative analysis and trap-induced variability *IEEE Trans. Electron Devices* **60** 2802–7

[10] Conzatti F, Pala M G and Esseni D 2012 Surface-roughness-induced variability in nanowire InAs tunnel FETs *IEEE Electron Device Lett.* **33** 806–8

[11] Brocard S, Pala M G and Esseni D 2013 Design options for hetero-junction tunnel FETs with high on current and steep sub-threshold voltage slope 1–5

[12] Sarkar D *et al* 2015 A subthermionic tunnel field-effect transistor with an atomically thin channel *Nature* **526** 91–5

[13] Li M, Esseni D, Snider G, Jena D and Xing H G 2014 Single particle transport in two-dimensional heterojunction Interlayer tunneling field effect transistor *J. Appl. Phys.* **115** 074508

[14] Das S, Prakash A, Salazar R and Appenzeller J 2014 Toward low-power electronics: tunneling phenomena in transition metal dichalcogenides *ACS Nano* **8** 1681–9

[15] Ilatikhameneh H, Tan Y, Novakovic B, Klimeck G, Rahman R and Appenzeller J 2015 Tunnel field-effect transistors in 2D transition metal dichalcogenide materials *IEEE J. Explor. Solid-State Comput. Devices Circuits* **1** 12–8

[16] Drögeler M *et al* 2014 Nanosecond spin lifetimes in single- and few-layer graphene–hBN heterostructures at room temperature *Nano Lett.* **14** 6050–5

[17] Ling X *et al* 2016 Parallel stitching of 2D materials *Adv. Mater.* **28** 2322–9

[18] Liu Z *et al* 2013 In-plane heterostructures of graphene and hexagonal boron nitride with controlled domain sizes *Nat. Nanotechnol.* **8** 119–24

[19] Sutter P, Cortes R, Lahiri J and Sutter E 2012 Interface formation in monolayer graphene-boron nitride heterostructures *Nano Lett.* **12** 4869–74

[20] Zhao M *et al* 2016 Large-scale chemical assembly of atomically thin transistors and circuits *Nat. Nanotechnol.* **11** 954–9

[21] Chen K *et al* 2015 Electronic properties of MoS_2–WS_2 heterostructures synthesized with two-step lateral epitaxial strategy *ACS Nano* **9** 9868–76

[22] Gong Y *et al* 2014 Vertical and in-plane heterostructures from WS_2/MoS_2 monolayers *Nat. Mater.* **13** 1135–42

[23] Aras M, Kılıç Ç and Ciraci S 2017 Planar heterostructures of single-layer transition metal dichalcogenides: composite structures, Schottky junctions, tunneling barriers, and half metals *Phys. Rev.* B **95**

[24] Fan Z-Q *et al* 2017 In-plane Schottky-barrier field-effect transistors based on 1 $T/2$ H heterojunctions of transition-metal dichalcogenides *Phys. Rev.* B **96**

[25] Fang S, Carr S, Shen J, Cazalilla M A and Kaxiras E 2018 Electronic structure theory of strained two-dimensional materials *Phys. Rev.* B **98** 075106

[26] Rasmussen F A and Thygesen K S 2015 Computational 2D materials database: electronic structure of transition-metal dichalcogenides and oxides *J. Phys. Chem.* C **119** 13169–83

[27] Kang J, Tongay S, Zhou J, Li J and Wu J 2013 Band offsets and heterostructures of two-dimensional semiconductors *Appl. Phys. Lett.* **102** 012111
[28] Gong C, Zhang H, Wang W, Colombo L, Wallace R M and Cho K 2013 Band alignment of two-dimensional transition metal dichalcogenides: application in tunnel field effect transistors *Appl. Phys. Lett.* **103** 053513
[29] Perdew J P 2009 Density functional theory and the band gap problem *Int. J. Quantum Chem.* **28** 497–523
[30] Zhang C *et al* 2018 Strain distributions and their influence on electronic structures of WSe_2–MoS_2 laterally strained heterojunctions *Nat. Nanotechnol.* **13** 152–8
[31] Fang S, Kuate Defo R, Shirodkar S N, Lieu S, Tritsaris G A and Kaxiras E 2015 *Ab initio* tight-binding Hamiltonian for transition metal dichalcogenides *Phys. Rev.* B **92** 205108
[32] Lopez Sancho M P, Lopez Sancho J M and Rubio J 1984 Quick iterative scheme for the calculation of transfer matrices: application to MO(100) *J. Phys.* F **14** 1205–15
[33] Ferry D K, Goodnick S M and Bird J P 2009 *Transport in Nanostructures* 2nd edn (Cambridge, New York: Cambridge University Press)
[34] Anantram M P, Lundstrom M S and Nikonov D E 2008 Modeling of nanoscale devices *Proc. IEEE* **96** 1511–50
[35] Yoon Y, Ganapathi K and Salahuddin S 2011 How good can monolayer MoS_2 transistors Be? *Nano Lett.* **11** 3768–73
[36] Jin Z, Li X, Mullen J T and Kim K W 2014 Intrinsic transport properties of electrons and holes in monolayer transition-metal dichalcogenides *Phys. Rev.* B **90** 045422
[37] Kaasbjerg K, Thygesen K S and Jacobsen K W 2012 Phonon-limited mobility in n-type single-layer MoS_2 from first principles *Phys. Rev.* B **85** 115317
[38] Kaasbjerg K, Thygesen K S and Jauho A-P 2013 Acoustic phonon limited mobility in two-dimensional semiconductors: deformation potential and piezoelectric scattering in monolayer MoS_2 from first principles *Phys. Rev.* B **87** 235312
[39] Wang X, Feng H, Wu Y and Jiao L 2013 Controlled synthesis of highly crystalline MoS_2 flakes by chemical vapor deposition *J. Am. Chem. Soc.* **135** 5304–7
[40] Lin Z *et al* 2016 Controllable growth of large–size crystalline MoS_2 and resist-free transfer assisted with a Cu thin film *Sci. Rep.* **5**
[41] Lam K-T, Cao X and Guo J 2013 Device performance of heterojunction tunneling field-effect transistors based on transition metal dichalcogenide monolayer *IEEE Electron Device Lett.* **34** 1331–3
[42] Liu F, Wang J and Guo H 2015 Negative differential resistance in monolayer WTe_2 tunneling transistors *Nanotechnology* **26** 175201